



## Full Text View

[Volume 29, Issue 1 \(January 1999\)](#)

### Journal of Physical Oceanography

Article: pp. 39–54 | [Abstract](#) | [PDF \(370K\)](#)

# The Establishment of the Tsugaru and the Alboran Gyres

**Doron Nof**

*Department of Oceanography and the Geophysical Fluid Dynamics Institute, The Florida State University, Tallahassee, Florida*

**Thierry Pichevin**

*Service Hydrographique et Oceanographique de la Marine, Brest, France*

(Manuscript received August 11, 1997, in final form February 25, 1998)

DOI: 10.1175/1520-0485(1999)029<0039:TEOTTA>2.0.CO;2

### ABSTRACT

A new theory for the generation of the Tsugaru and Alboran gyres is proposed. The essence of the theory can be described as follows. Using the nonlinear reduced-gravity (shallow water) equations, it has been recently shown by Pichevin and Nof that a channel emptying light water into an otherwise resting ocean of denser water on an  $f$  plane produces a forever-growing gyre next to the channel mouth. The generation of the gyre is caused by the (otherwise imbalanced) flow force of the alongshore current downstream regardless of the initial current vorticity. [By changing the potential vorticity via friction, the fluid creates the required vorticity (on its own) in the cases where the incoming flow has a vorticity that cannot accommodate the gyre.]

It is shown here, analytically and numerically, that when the channel is oriented eastward (i.e., the channel is situated along a western boundary as is the case with the Tsugaru and Alboran gyres) the presence of  $\beta$  causes an *arrest* of the gyre's growth. As a result, a steady state corresponding to a flow field resembling a snail is established. Here, the "shell" of the imaginary snail corresponds to the gyre and the elongated body of the snail corresponds to the downstream current. The establishment of the modeled steady gyre is inevitable, regardless of the upstream potential vorticity, and the gyre has a length scale involving both  $\beta$  and the Rossby radius.

The analytical solution to the inviscid nonlinear equations is constructed using a perturbation scheme in  $\epsilon$ , the ratio of the Coriolis parameter variation across the current to the Coriolis parameter at the center. It shows that the gyre size is roughly  $2R_d \epsilon^{1/4}$  [where  $R_d$  is the Rossby radius (based on the downstream thickness  $H$ ) and  $\epsilon \equiv \beta R_d / f_0$ ] implying that the Tsugaru and the Alboran gyres have a scale that is greater than the usual current scale ( $R_d$ ). Numerical

simulations, using the Bleck and Boudra model, are in excellent agreement with the theoretical prediction for the inviscid gyre size; they also show that the gyres are established regardless of the upstream potential vorticity. Both the analytical and the numerical results are in good agreement with the observations.

#### Table of Contents:

- [Introduction](#)
- [Formulation](#)
- [Scaling and expansion](#)
- [Solution](#)
- [Numerical simulations](#)
- [Limitations](#)
- [Discussion and summary](#)
- [REFERENCES](#)
- [APPENDIX](#)
- [TABLES](#)
- [FIGURES](#)

#### Options:

- [Create Reference](#)
- [Email this Article](#)
- [Add to MyArchive](#)
- [Search AMS Glossary](#)

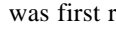
#### Search CrossRef for:

- [Articles Citing This Article](#)

#### Search Google Scholar for:

- [Doron Nof](#)
- [Thierry Pichevin](#)

## 1. Introduction

The question of what establishes the Alboran and the Tsugaru gyres has troubled oceanographers since their existence was first reported [by [Lacombe and Tchernia \(1972\)](#) and [Conlon \(1982\)](#)]. Both gyres ([Fig. 1](#) ) correspond to an eastward channel situated in the western boundary of the basin into which the flow debouches. The dimensions of the two gyres (50–100 km) are comparable and so are the transports [ $\sim O(1)$  Sv, see [Speich et al. \(1996\)](#) and [Yasuda et al. \(1988\)](#)]. The only two differences between the two gyres are that the Alboran is more or less a permanent gyre, whereas the Tsugaru breaks down during the cold months of the year, and there is a wall to the south of the gyre in the Alboran case.

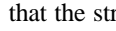
There are numerous articles on the Alboran gyre and its possible generation process [see, e.g., [Speich et al. \(1996\)](#) for a thorough review of previous theories]. Most of them state that negative vorticity must be present within the Strait of Gibraltar in order for the gyre to be established. The sole article that specifically addresses the Tsugaru gyre formation theoretically ([Kubokawa 1991](#)) also relies on the presence of low potential vorticity in the strait. Exceptions to these vorticity arguments are the studies of (i) [Whitehead and Miller \(1979\)](#) who pointed out that, once a jet separates from the coast and then reattaches itself to the coast, a growing gyre is inevitable; (ii) [Bormans and Garrett \(1989\)](#) who showed that a separation occurs whenever the Rossby number, based on the curvature of the exit, is less than unity; (iii) the studies of [Preller \(1986\)](#), [Werner et al. \(1988\)](#), and [Saint-Guilly \(1957\)](#) who suggest that the gyre might be a part of a standing Rossby wave; and (iv) the recent study of [Viúdez \(1997\)](#) who, on the basis of an earlier analysis that indicated that the relative vorticity of the Alboran jet is not negative ([Viúdez et al. 1996](#); [Viúdez and Haney 1997](#)), suggests that evaporation in the Eastern Mediterranean is responsible for the Alboran gyre formation.

All of these studies (as well as the many studies mentioned therein) are informative and useful but it is still not clear why the gyres are established. In this article, we shall specifically address the question why the gyres are established and suggest a new process for the generation of both gyres. Following [Pichevin and Nof \(1997\)](#) we shall show analytically in [section 2](#) that the formation of a gyre is a fundamental property of any eastward *outflow* regardless of the fluid's vorticity. It results from the impossibility to balance the flow force associated with the alongshore current without the establishment of a gyre.

Previous studies (e.g., [Nof 1986](#)) have shown that flow force (or momentum flux) is a more fundamental property than either energy or vorticity in the sense that conservation of momentum may require both the energy and vorticity to change. We shall see that a similar process takes place in the establishment of the gyres ([section 2](#)). Specifically, even an outflow with a cyclonic, rather than an anticyclonic relative vorticity, generates a gyre with an anticyclonic vorticity through the alteration of potential vorticity via friction. Using a perturbation expansion, we shall demonstrate analytically that the presence of  $\beta$  arrests the gyre's growth ([sections 3](#) and [4](#)). The arrest results from a balance between the southward  $\beta$ -induced force associated with the gyre and the northward flow force associated with the alongshore jet.

Using a numerical reduced-gravity model of the Bleck and Boudra type, we shall then show that, as the analytical solution predicts, the variation of the Coriolis parameter with latitude arrests the growth of the gyre ([section 5](#)). As a result, a permanent gyre with a radius of roughly  $2R_d/(\beta R_d/f_0)^{1/6}$  is established. The derivation of this solution as well as the proceeding numerical simulations are the main new aspects of this article. The limitations of our model are discussed in [section 6](#); detailed application of the models to the Tsugaru and Alboran gyres is discussed and the results are summarized in [section 7](#).

## 2. Formulation

This section describes the physics of the problem and the mathematical approach. Consider an eastward zonal channel carrying relatively light water (with density  $\rho$ ) emptying into an otherwise stagnant ocean (with density  $\rho + \Delta\rho$ ) and assume that the streamlines remain parallel to the channel wall until the opening (i.e., the channel mouth) is reached ([Fig. 2](#) ). In reality one would expect the streamlines to be somewhat curved a distance of up to  $O(W)$ , where  $W$  is the channel width, upstream from the mouth. This assumption implies that the channel width  $W$  is small compared to the gyre's scale so that the curvature of the flow at the mouth does not contribute to the momentum flux along the coast. We shall see later that this assumption essentially means that  $W \ll R_d \varepsilon^{1/4}$  (where  $R_d$  is the current downstream Rossby radius,  $\varepsilon \equiv \beta R_d/f_0$ , and  $R_d/\varepsilon^{1/4}$  is the gyre's Rossby radius; here,  $\beta$  is the familiar linear variation of the Coriolis parameter with latitude and  $f_0$  is the Coriolis parameter), implying that the Burger number is large.

The reader who is concerned about the validity of this assumption is referred to [Pichevin and Nof \(1997\)](#) and [Nof \(1988, Fig. 4 and pages 188–191\)](#) where it is shown that in the limit,  $W \rightarrow 0$ , the flow becomes symmetrical with respect to the  $x$  axis so that the contribution of the curved flow in the channel to the alongshore momentum flux (in conventional notation)  $\int_A^B hu \nu dx$  goes to zero. This assumption of parallel streamlines at the mouth is reasonable and has been used before in many similar problems (see, e.g., [Nof, 1978a,b](#); [1981](#); [1996](#)). However, it filters out the regime where the Burger number is small ( $W \gg R_d \varepsilon^{1/4}$ ), a regime frequently associated with a no-gyre situation (see, e.g., [Whitehead and Miller 1979](#); [Bormans and Garrett 1989](#); [Kawasaki and Sugimoto 1984](#); [Gliezon et al. 1996](#)). We shall return to this important point later.

The region immediately to the right of corner B, which is a point of infinite speed (see, e.g., [Batchelor 1967](#)), might involve a separation from the wall and reattachment (see, e.g., [Cherniawsky and LeBlond 1986](#)), but whether or not such a

separation exists has no bearing on our calculations.

As the light current exits the channel it must turn to the right and hug the coast because this is where Kelvin waves will propagate to and this is the only place where such a current can have a finite cross-sectional area. Assuming that a steady state can be reached and integrating the steady nonlinear y momentum equation over the fixed region  $S$  bounded by the dashed line ABCDEFA shown in [Fig. 2](#), we get

$$\begin{aligned} & \iint_S \left( hu \frac{\partial v}{\partial x} + hv \frac{\partial v}{\partial y} \right) dx dy \\ & + \iint_S (f_0 + \beta y) uh dx dy \\ & + \frac{g'}{2} \iint_S \frac{\partial}{\partial y} (h^2) dx dy = 0, \end{aligned} \quad (2.1)$$

which by using the continuity equation and streamfunction  $\psi$  can be reduced to

$$\begin{aligned} & \iint_S \left[ \frac{\partial}{\partial x} (huv) + \frac{\partial}{\partial y} (hv^2) \right] dx dy \\ & - \iint_S (f_0 + \beta y) \frac{\partial \psi}{\partial y} dx dy \\ & + \frac{g'}{2} \iint_S \frac{\partial (h^2)}{\partial y} dx dy = 0. \end{aligned} \quad (2.2)$$

Here, the notation is conventional, that is,  $u$  and  $v$  are the horizontal velocity components in the  $x$  and  $y$  direction,  $h$  the thickness of the upper layer,  $\psi$  a streamfunction defined by  $\partial \psi / \partial y = -uh$ ;  $\partial \psi / \partial x = vh$ , and  $g'$  is the reduced gravity,  $g\Delta\rho/\rho$ . For convenience, all variables are defined both in the text and in the appendix.

[Equation \(2.2\)](#) can be rewritten as

$$\begin{aligned} & - \iint_S \left[ \frac{\partial}{\partial x} (huv) + \frac{\partial}{\partial y} (hv^2) \right] dx dy - \iint_S f_0 \frac{\partial \psi}{\partial y} dx dy - \iint_S \left[ \frac{\partial}{\partial y} (\beta y \psi) - \beta \psi \right] dx dy \\ & + \frac{g'}{2} \iint_S \frac{\partial}{\partial y} (h^2) dx dy = 0, \end{aligned} \quad (2.3)$$

*(Click the equation graphic to enlarge/reduce size)*

and application of Stokes theorem to [\(2.3\)](#) gives

$$\oint_{\Phi} huv dy - \oint_{\Phi} (hv^2 + g'h^2/2) dx - f_0 \oint_{\Phi} \psi dx + \beta \oint_{\Phi} y\psi dx + \beta \iint_S \psi dx dy = 0, \quad (2.4)$$

*(Click the equation graphic to enlarge/reduce size)*

where  $\Phi$  is the boundary of  $S$  and the arrowed circles indicate counterclockwise integration.

Next, we define  $\psi$  to be zero along the front ( $h = 0$ ) and note that at least one of the three variables  $h$ ,  $u$ , and  $v$  vanishes on every portion of the boundary  $\Phi$ , so [\(2.4\)](#) can be rearranged and written as

$$\int_C^D [hv^2 + g'h^2/2 - (f_0 + \beta y)\psi] dx - \beta \iint_S \psi dx dy = 0. \quad (2.5)$$

Assuming (and later verifying with our numerical experiments) that the downstream flow is parallel to the wall and, hence, geostrophic in CD [so that  $(f_0 + \beta y)\mathbf{v} = g'\partial h/\partial x$  which, upon multiplication by  $h$  and integration in  $x$  from a point within the current to its edge, where  $\Psi = h = 0$ , gives  $(f_0 + \beta y)\Psi = g'h^2/2$ ], relation (2.5) reduces to the simple relationship,

$$\int_0^L hv^2 dx - \beta \iint_S \psi dx dy = 0, \quad (2.6)$$

where  $L$  is the width of the current downstream.

Equation (2.6) represents a balance between two forces. The first is a northward force associated with the alongshore current. It is analogous to the force produced by a rocket or a sprinkler. The second is a southward  $\beta$  force resulting from the fact that as a particle circulates in a clockwise manner within the gyre it senses a larger Coriolis force on the north side than it senses on the south side.

The curious result is that, when  $\beta \equiv 0$ , condition (2.6) cannot be satisfied because  $v^2$  is always positive along CD and the integration is done from small to large  $x$ . The impossibility to satisfy (2.6) with  $\beta \equiv 0$  implies that on an  $f$  plane there cannot be a steady state because the integrated momentum (or flow force) imparted by the fluid exiting through CD on the control volume bounded by ABCDEF cannot be balanced. This  $f$ -plane case was already discussed in [Pichevin and Nof \(1997\)](#) and need not be repeated here. It is sufficient to say that, according to their  $f$ -plane analysis, a forever-growing gyre is established near the mouth. The gyre is constantly growing because the curving flow bifurcates as it impinges on the wall. Namely, as a result of the bifurcation, part of the flow turns backwards causing the volume of the gyre to constantly grow.

On a  $\beta$  plane, the situation is quite different because the gyre's growth causes a steady increase in the southward force  $\beta \iint \Psi dx dy$ . This increasing southward  $\beta$  force ultimately balances the northward flow force associated with the southward current downstream, implying that the role of  $\beta$  in this case is merely to arrest the growth of the gyre.

The above balance of forces holds regardless of the fluid's potential vorticity. When the incoming relative vorticity is not negative enough to permit the establishment of the anticyclonic gyre,<sup>1</sup> something else must adjust to produce the gyre. We shall see that friction comes in and alters the potential vorticity until the necessary vorticity is created. However, when the channel is oriented westward instead of eastward, the downstream current must flow northward and, consequently, the two terms in (2.6) are of the same sign and can never balance each other. As a result, a steady state cannot be reached and a convoluted periodic detachment of eddies is established (see [Pichevin 1996](#), his Fig. 5.2).

Before proceeding it is appropriate to point out that the above balance of forces may not exist in the case of a curved coastline, a curved strait, or a topography that depends on  $y$  because under such conditions the flow force may be exerted on the wall rather than the fluid. We shall return to this important point in [section 6](#).

### 3. Scaling and expansion

#### a. Scales

We shall now show that the balance previously discussed implies that the gyre scale is inversely proportional to  $\beta$  and that its length scale ( $R_{dg}$ ) is greater than the current's length scale  $R_d$ . (Note that the subscript  $g$  indicates association with the gyre). To see this, note that a comparison of the two terms in (2.6) gives,

$$H \cdot R_d \cdot g' H_g^2 \sim O\left(\beta R_{dg}^2 \cdot \frac{g' H_g^2}{f}\right),$$

which, together with the condition  $(H/H_g^2) = (R_d/R_{dg})^4$ , yields,

$$R_{dg} \sim O(R_d/\epsilon^{1/4}), \quad (3.1)$$

where  $\varepsilon \equiv \beta R_d f_0 \ll 1$ . Thus, the gyre's scale is inversely proportional to  $\beta^{1/4}$ . In deriving the above scale it has been taken into account that, due to the Bernoulli integral, the speed along the gyre edge ( $h = 0$ ) is the same as the speed along the downstream current edge.

Two comments should be made with regard to (3.1). First, as is frequently the case, the scaling may conceal potentially large numbers such as powers of the known  $2(2)^{1/2}$  ratio between the gyre minimum radius and the Rossby radius (see, e.g., [Nof 1981](#); [Killworth 1983](#)). Second, the  $1/4$  power of  $\varepsilon$  implies that, for most cases,  $R_{dg}$  will not be greatly different from  $R_d$  (though it will be larger).

Given the above scales we now introduce the following nondimensional parameters. For the alongshore current leaving the control volume through CD, denoted by the subscript  $l$ , the scaled variables are

$$\begin{aligned} x_l^* &= x/R_d; & y_l^* &= y/R_d; & v_l^* &= v/(g'H_g)^{1/2} \\ h_l^* &= h/H; & R_d &\equiv (g'H)^{1/2}/f_0. \end{aligned} \quad (3.2)$$

Similarly, the scaled variables for the gyre are

$$\begin{aligned} x_g^* &= x/R_{dg}; & y_g^* &= y/R_{dg}; & h_g^* &= \frac{h}{H \left( \frac{R_{dg}}{R_d} \right)^2} \\ R_{dg} &= R_d/\varepsilon^{1/4}; & \varepsilon &\equiv \beta R_d/f_0 \ll 1; \\ \psi_g^* &= \frac{\psi}{(g'H_g^2/f_0)}, \end{aligned} \quad (3.3)$$

where  $R_{dg}$  is not necessarily based on the gyre maximum depth but rather is merely a length scale for the gyre.

The above scaling implies that the ratio of the gyre's depth to the parent current depth is  $O(\varepsilon^{1/2})$ , which means that the gyre is deeper than the current. Since, in the mean, the gyre must have an anticyclonic vorticity, the inviscid parent current must also have anticyclonic vorticity. Furthermore, this anticyclonic vorticity must be large so that it can compensate for the stretching of the water columns that occurs during the gyre formation. Of course, one can think of parent currents with cyclonic rather than anticyclonic vorticity and we shall show later (with the aid of our numerical experiments) that through the action of small friction the potential vorticity of a (parent) cyclonic current is gradually altered so that an anticyclonic gyre is produced.

### b. The nondimensional equations

Substitution of (3.2) and (3.3) into the integrated momentum (2.6) gives

$$\int_0^{L^*} h_l^* (v_l^*)^2 dy_l^* + \iint_S \psi_g^* dy_g^* dx_g^* = 0. \quad (3.4)$$

Similarly, the continuity equation can be written as

$$Q^* = \int_0^{L^*} h_l^* v_l^* dx_l^*, \quad (3.5)$$

where  $Q^*$  is the known nondimensional mass flux out of the channel, defined by  $Q/[g'H^2/f_0]$ . Recall that, in addition to the above two equations, the field is governed by the potential vorticity equation and the steady Bernoulli principle. We shall shortly see that these will enable us to close the inviscid problem.

### c. Expansions

To obtain the solution, all the dependent variables of the gyre are now expanded in a power series in  $\varepsilon^{1/6}$ , for example,

$$\left. \begin{aligned} h_g^* &= h_g^{(0)} + \varepsilon^{1/4} h_g^{(1)} + \dots \\ \psi_g^* &= \psi_g^{(0)} + \varepsilon^{1/4} \psi_g^{(1)} + \dots \\ v_i^* &= v_i^{(0)} + \varepsilon^{1/4} v_i^{(1)} + \dots \\ h_i^* &= h_i^{(0)} + \varepsilon^{1/4} h_i^{(1)} + \dots \end{aligned} \right\} \quad (3.6)$$

The expansion implies that the gyre's circular basic state is subject to a perturbation of  $O(\varepsilon^{1/4})$ . This reflects the condition that the deviation of the gyre from a circular shape is proportional to the current's width downstream.

Substitution of (3.6) into (3.4) and (3.5) gives the following leading-order balance:

$$\int_0^{L^{(0)}} h_i^{(0)} (v_i^{(0)})^2 dx_i^* = \iint \psi_g^{(0)} dx_g^* dy_g^*. \quad (3.7a)$$

$$Q^* = \int_0^{L^{(0)}} h_i^{(0)} v_i^{(0)} dx_i^* \quad (3.7b)$$

Equation (3.7a) implies that the flow force associated with the downstream current is balanced by the  $\beta$  force applied to a circular  $f$ -plane gyre.

#### 4. Solution

As mentioned, since our scaling implies that the gyres must be deeper than the parent current [ $H_g \sim O(H/\varepsilon^{1/2})$ ], it follows that, in the inviscid case, the parent current must have strong anticyclonic vorticity, that is, the gyre's vorticity will be anticyclonic (despite the severe stretching of the water column that occurs during its formation) only if the parent current vorticity is strongly anticyclonic. What happens when the parent current vorticity is not strongly anticyclonic? As mentioned, we shall see later that, since the momentum flux (i.e., the flow force) is a more fundamental property than the vorticity, friction becomes very important when necessary and changes the potential vorticity so that it can accommodate the required balance and resulting formation of the gyre.

##### a. Zero potential vorticity gyres

We shall first look at the case where both the incoming current and the gyre have zero potential vorticity because it is the simplest possible case. Note that such a situation is established whenever the upstream basin from which the fluid originates is much deeper than the sill depth. Under such conditions, the solutions for both the alongshore current and the zeroth-order gyre are straightforward despite the nonlinearity. Specifically, the leading-order solution for the alongshore downstream current is

$$\left. \begin{aligned} v &= V_l + \dots \\ h &= V_l(L - x) \frac{f_0}{g'} + \dots \end{aligned} \right\}, \quad (4.1)$$

where  $V_l$  is the near-wall speed,  $L$  is the alongshore current width, and, for simplicity, we have returned to dimensional variables. Hence, the alongshore current near-wall depth  $H_l$  is

$$H_l = f_0 L \frac{V_l}{g'} + \dots \quad (4.2)$$

Note that the application of the Bernoulli principle to the wall on the right-hand side gives

$$\left[ \frac{1}{2}(U^2) + g'H \right] = \frac{1}{2}(V_l)^2, \quad (4.3)$$

where both  $U$  and  $H$  are known upstream parameters near the right bank.

Similarly, the leading-order solution for the zero potential vorticity gyre is

$$\left. \begin{aligned} \bar{v}_{\theta g} &= -fr/2 \\ \bar{h}_g &= \frac{f_0^2}{8g'} \left( \frac{8g'h}{f_0^2} - r^2 \right) \end{aligned} \right\}, \quad (4.4)$$

where, for simplicity, we use here a polar coordinate system  $(r, \theta)$  whose origin coincides with the center of the gyre;  $\hat{h}_g$  is the gyre's maximum depth; and the bars  $(-)$  denote association with the zeroth-order circular state. The above general solution has one unknown: the gyre's maximum depth at the center  $\hat{h}_g$ .

Leaving the derivation of the general solution aside for a moment, we note that insertion of the nondimensional form of (4.1)–(4.3) into (3.5) gives the straightforward solution for the downstream current,

$$Q^* = (L^*)^2 \frac{(V_i^*)^2}{2}, \quad (4.5)$$

where  $V_i^*$ , the alongshore current near-wall speed, is given by

$$V_i^* = (2B^*)^{1/2}, \quad (4.6)$$

where, to avoid flow reversals, the positive root was chosen. Here  $B^*$  is the *known* upstream Bernoulli relation  $(U^2/2 + g'H)$  along the right wall, nondimensionalized by  $g'H$  (which is also known). Equations (4.5) and (4.6) can be combined to give

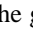
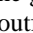
$$L^* = (2Q^*)^{1/2}/2B^*. \quad (4.7)$$

We now return to the derivation of the general solution. Equation (4.5) together with the substitution of the zeroth-order solution (4.4), in nondimensional form, into (3.7) gives the desired solution in terms of the known upstream flux  $Q$  and the known Bernoulli energy along the upstream wall  $B$ . For zero potential vorticity the dimensional zeroth-order radius of the gyre  $R$  is given by

$$R = 20 \left( \frac{64}{5\pi} \right)^{1/4} \frac{R_d}{\varepsilon^{1/4}} \left( \frac{B}{g'H} \right)^{3/2} \left( \frac{Q}{g'H^2/f} \right)^{1/2} \quad (4.8)$$

and is shown graphically in Fig. 3 .

### b. Finite potential vorticity gyres

For finite potential flow the final calculations must be done numerically because there is no known analytical solution for the zeroth-order gyre (see, e.g., Flierl 1979). Such calculations were performed for the cases where the potential vorticity depth is 5% and 100% greater than the gyre's maximum depth (Fig. 3 ). These correspond to a relative vorticity of  $-0.05F$  and  $-0.5f$ , typical for many outflows. All of the presently shown cases (Fig. 3 ) correspond to upstream flows with sufficient anticyclonic vorticity to allow for the inviscid establishment of the gyres, that is, friction plays no role and potential vorticity is conserved. Note that the main difference between the zero and finite potential vorticity gyres is that in the finite potential vorticity case the gyre size is larger than that of the zero potential vorticity case.

## 5. Numerical simulations

To further analyze the validity of our assumptions (e.g., that the flow is parallel to the wall downstream) and examine what happens when the upstream vorticity is cyclonic, numerical simulations were performed and the results were quantitatively analyzed.

### a. Numerical model description

We used the Bleck and Boudra (1986) reduced-gravity isopycnic model with a passive lower layer and employed the Orlandi (1976) second-order radiation conditions for the open boundary in the south. We shall see later that this condition is satisfactory because the downstream streamlines are not disturbed when they cross the boundary. Also, placing the boundary in different locations did not alter our results. To speed up the experiments and make our runs economically feasible, we sometimes used a magnified value for  $\beta$ . For the same reason, we also took a transport of roughly 17.5 Sv (Sv  $\equiv 10^6 \text{ m}^3 \text{ s}^{-1}$ ), an order of magnitude larger than the actual transports. These choices were unavoidable; since our final plots are nondimensional, the discrepancy between the actual and the modeled variables is tolerable.

In accordance with the above choices, our grid size was 15 km, which is adequate for processes where the Rossby radius is roughly 30 km. It would, of course, have been better to use a higher resolution but our computing time was limited and, consequently, we could only perform a limited number of experiments. Our time step was 1500 s and, for numerical stability, we introduced a small (horizontal) Laplacian friction of  $\nu = 3 \times 10^6 \text{ cm}^2 \text{ s}^{-1}$ . Our walls were slippery and, as is usually the case, we took the vorticity to be zero next to the walls. As is typical for the Tsugaru Strait and the Alboran gyre, we took  $f_0 = 10^{-4} \text{ s}^{-1}$  and  $g'$  of roughly  $1.4 \text{ cm s}^{-2}$ .

### b. General results

We show a total of eight experiments with an eastward channel emptying into an infinite ocean (Table 1) and three additional experiments with a channel discharging into an ocean with a corner (to simulate the African continent). In five of the first eight experiments (1, 4, 6, 7, and 8) the initial relative vorticity was negative enough to directly allow the establishment of the anticyclonic gyre. The initial relative vorticity of the remaining three experiments (2, 3, and 5) was either cyclonic or weakly anticyclonic so that the stretching associated with the formation of the gyre forced an alteration of the potential vorticity which occurred through the action of horizontal friction. The general features described by our analytical theory are clearly present in our numerical simulations. In all of our experiments the flow becomes steady, turns to the right (southward) after leaving the channel, and, as expected, forms a gyre (Fig. 4); the lower panels of Fig. 4 show that the assumed steadiness and the corresponding balance of forces are indeed achieved. Furthermore, the experiments where the initial upstream vorticity was not negative enough to permit the establishment of the gyre show a clear alteration of the potential vorticity (Figs. 5 and 6).

A comparison of the analytical prediction for the gyre's radius to the numerical no-potential-vorticity-alteration cases (i.e., negligible friction) shows (Fig. 7) excellent agreement, with errors no more than 11%. This is remarkable considering that  $\epsilon^{1/4}$  is relatively large ( $\sim 0.4$ ); it results from the integration which is not very sensitive to the gyre's shape. (Note that a comparison of the analytical results to the cases where the potential vorticity is changing, as one follows a particle, has no meaning because our analytical results are not supposed to be valid in these cases.)

### c. The influence of a southern wall

We also examined the effect of a southern zonal wall (to simulate the influence of the African coast on the Alboran gyre) and noted that, although its presence altered the structure of the gyre, it does not prevent its establishment. Figure 8 shows the general structure of the flow in this case. Assuming (and later verifying with our numerical experiments) that the flow is parallel to the southern wall downstream (so that  $\mathbf{v} \equiv 0$  across DE), we find that (2.6) is modified to

$$\frac{g'}{2} \int_c^D h^2 dx = \int_c^D [(f_0 + \beta y)\psi] dx + \beta \iint \psi dx dy. \quad (5.1)$$

Here, all terms are positive and the first term on the right-hand side is simply the integral of the known transport along the wall, that is, the balance states that the gyre's growth is arrested when the northward force exerted by the wall compensates for the southward  $\beta$  force. Equation (5.1) shows that a steady state corresponding to a gyre is still possible but, in contrast to the no-zonal-wall case, it is impossible to determine the scale of the gyre. This is because a priori it is difficult to estimate the difference between the term on the left and the first term on the right. All that we know is, since the velocity is zero in the corner (point C), the thickness  $h$  is relatively large there because of the Bernoulli effect. Numerical experiments (Fig. 9) clearly illustrate, however, that a gyre is indeed established.

## 6. Limitations

As is frequently the case, both the analytical and the numerical model have their limitations. The two most important ones result from the parallel streamlines at-the-mouth assumption and the use of a layer-and-a-half model. We shall address these issues one by one.

The first assumption eliminates the contribution of the curved flow in the channel to the alongshore momentum flux because the (assumed) straight streamlines are perpendicular to the coast. The assumption has been used successfully before (e.g., Nof 1978a,b; 1981), and Nof (1988, his Fig. 4, 188–191) has shown that it is valid as long as the channel width is narrow compared to the outflow length scale. However, although the assumption is reasonable, it essentially excludes the effects of the strait curvature and shape from the model. Thus, it eliminates the possibility that some of the momentum flux associated with the alongshore downstream current be balanced by a pressure force exerted on the fluid by the channel walls instead of being balanced by the  $\beta$ -induced force associated with the gyre.

On this basis one would expect that the excluded regime may not always involve a gyre. Indeed, as has been shown by Whitehead and Miller (1979), Kawasaki and Sugimoto (1984), Bormans and Garrett (1989), and Gliezon et al. (1996), the



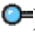
excluded regime [of a small Burger number, that is, a small ratio between the channel width (or curvature) and the length scale of the flow immediately to the east of the mouth] is often associated with a no-gyre situation. We shall see shortly that in both the Alboran and the Tsugaru cases the length scale of the flow outside the channel is indeed greater than the channel width, indicating that the parallel streamlines at-the-mouth assumption is justified. However, in both situations we are not very far from the excluded regime.


We shall also see shortly that the observed seasonal breakdown of the Tsugaru gyre is most likely not related to the excluded regime. Similarly, it appears that the occasional breakdown of the Alboran gyre ([Heburn and La Violette 1990](#); [Perkins et al. 1990](#)) is not associated with the flow transition from one regime to another because the flow's Rossby radius seems to increase during the no-gyre state. This completes our discussion of the parallel streamline at-the-mouth assumption.

Our second limitation resulting from the one-and-a-half layer approach excludes baroclinic instabilities of both the gyre and the downstream current. Consequently, the cyclonic eddies noted along the rim of the gyre in both laboratory experiments ([Gliezon et al. 1996](#)) and numerical models ([Speich 1996](#)) are not present in our numerical experiments. It is noted here in passing that such cyclones are also observed along the periphery of other anticyclonic features such as warm core rings ([Kennelly et al. 1985](#); [Nof 1993](#)).


## 7. Discussion and summary



The foregoing theory is applicable to numerous situations because many oceans and marginal seas are connected to each other by zonal channels. The cases of zonal eastward channels for which there are the most data available on both the origin of the flow and its final fate are the Tsugaru and Alboran gyres. For this reason, we shall attempt to compare our results to the way that these two gyres are formed. Both the flow through the Tsugaru and the Strait of Gibraltar carry roughly 1 Sv of light water into the corresponding basins.

Our present theory suggests that, without the generation of the gyres, the momentum associated with the southward flow downstream of the straits could not have been balanced. It implies that the gyres are generated in order to offset the flow force associated with the southward turning jets. For the Alboran gyre we chose the following numerical values:  $g' \approx 1.5 \times 10^{-2} \text{ m s}^{-2}$ ;  $H \approx 100 \text{ m}$ ;  $f \approx 10^{-4} \text{ s}^{-1}$ , and  $\beta \approx 2 \times 10^{-11} \text{ s}^{-1} \text{ m}^{-1}$ . These values correspond to a transport of roughly 1 Sv, a Rossby radius of 12 km, and an  $\epsilon^{1/4}$  of 0.25. Because of the tendency of nonlinear frontal models such as ours, to produce large speeds along the front (see, e.g., [Flierl 1979](#)), we have chosen here a relatively low value for  $g'$ . Our predicted analytical radius of the Alboran gyre ( $\approx 2R_d/\epsilon^{1/6}$ ) is 87 km, which agrees with the observations (see, e.g., [Viúdez 1997](#) and [Fig. 1](#) ) fairly well even though it ignores the influence of the southern wall. The parallel streamlines at-the-mouth assumption is adequate because the gyre's Rossby radius (27 km) is larger than the strait width ( $\sim 15 \text{ km}$ ). Note that it is not clear to what the observed occasional disappearance of the gyre ([Heburn and La Violette 1990](#); [Perkins et al. 1990](#)) is related.

For the Tsugaru Strait the situation is somewhat more complicated because of the bimodal structure. The Tsugaru gyre is only observed during the warm months of the year when the Rossby radius is relatively large ( $\sim 23 \text{ km}$  according to [Conlon 1982](#)). It is asserted here that, when the gyre is not observed (the cold months), the relatively small Rossby radius (10 km or less according to [Conlon 1982](#)) prevents the flow in the strait from sensing the left channel bank, which is situated roughly 20 km away. Under such conditions, the flow does not even “know” that there is a channel and, consequently, it simply follows the coastline on the right without forming a gyre. During the warm months when the flow in the strait touches both banks and the gyre is formed, the parameter  $\epsilon^{1/4}$  is 0.46 and the analytically predicted radius ( $2R_d/\epsilon^{1/4}$ ) is 110 km. This is also in good agreement with the observations (see [Fig. 1](#) ). As in the Alboran gyre case, the parallel streamlines at-the-mouth assumption is adequate because the (warm) gyre's Rossby radius (38 km) is greater than the strait width (20 km). Of the two applications, the one to the Tsugaru is probably more adequate because there is no southern boundary there and the influence of  $\beta$  is more pronounced (due to the larger north–south extent).

A comment should be made here regarding the observed vorticity of the flow in the Gibraltar and Tsugaru Straits. Presently, it is impossible to tell from the observations what the actual vorticity is but since the flow speeds up and shoals as it enters the straits suggests (via conservation of potential vorticity) that it is anticyclonic. Whether this (unknown) negative vorticity is strong enough to produce a gyre without the alteration of potential vorticity is, of course, not known; it is a subject for future investigations. We have seen, however, that a gyre is established regardless of the initial vorticity.

In summary, it can be said that the primary aim of our theory and numerical experiments was to examine a new gyre generation mechanism that is related to the flow force of a current exiting from an eastward oriented channel. The new inviscid generation process implies that a light current exiting from a channel perpendicular to the coastline ([Fig. 2](#) ) exerts a flow force (parallel to the wall) that cannot be balanced without the generation of a gyre on the opposing side. With a gyre present, however, the northward flow force of the downstream current is balanced by the southward  $\beta$ -induced force associated with the anticyclonic flow in the gyre.

Using an integrated momentum technique, we have computed analytically the structure of the resulting gyre ([Fig. 3](#) ). A new length scale for gyres emerges from our calculations. Quantitative numerical simulations ([Figs. 4–8](#) ) show the generation process in detail and verify the analytical prediction. Finally, we applied our model to the Tsugaru and Alboran gyres and argue that the predictions regarding the gyre size are in good agreement with observations and that the generation

of these gyres is inevitable.

The generation of the gyres is not inevitable, however, in the cases where the parallel streamlines assumption at the mouth is violated ( $R_d/\epsilon^{1/4} \approx W$ ), that is, when the width and curvature of the channel is of the same order as the gyre's Rossby radius. In these cases, the northward flow force associated with the alongshore downstream current may be balanced by a pressure force exerted on the fluid by the channel side walls rather than by the  $\beta$ -induced force associated with the gyre.

#### Acknowledgments

This study was supported by the National Science Foundation under Contracts OCE 9503816 and 9633655, National Aeronautics and Space Administration Grants NAGW-4883 and NAG5-4613, and Office of Naval Research Grant N00014-89-J-1606. T. Pichevin was funded by Service Hydrographique et Océanographique de la Marine (SHOM) and this work is based in part on his Ph.D. dissertation. We had useful discussions with G. Weatherly and W. Sturges. Computations were carefully checked by S. Van Gorder.

---

#### REFERENCES

- Batchelor, G. K., 1967: *An Introduction to Fluid Dynamics*. Cambridge University Press, 615 pp..
- Bleck, R., and D. Boudra, 1986: Wind-driven spin-up in eddy-resolving ocean models formulated in isopycnic and isobaric coordinates. *J. Geophys. Res.*, **91**, 7611–7621..
- Bormans, M., and C. Garrett, 1989: A simple criterion for gyre formation by the surface outflow from a strait, with application to the Alboran Sea. *J. Geophys. Res.*, **94**, 12 637–12 644..
- Cherniawsky, J., and P. H. LeBlond, 1986: Rotating flows along indented coastlines. *J. Fluid Mech.*, **169**, 379–407..
- Conlon, D. M., 1982: On the outflow modes of the Tsugaru warm current. *La Mer*, **20**, 60–64..
- Flierl, G., 1979: A simple model of the structure of warm and cold-core rings. *J. Geophys. Res.*, **84**, 78–85..
- Gliezon, P., G. Chabert D'Hieres, and D. Renouard, 1996: Experimental study of the Alboran Sea gyres. *Oceanol. Acta*, **19**, 499–511..
- Heburn, G. W., and P. La Violette, 1990: Variations in the structure of the anticyclonic gyres found in the Alboran Sea. *J. Geophys. Res.*, **95**, 1599–1613..
- Kawasaki, Y., and T. Sugimoto, 1984: Experimental studies on the formation and degeneration processes of the Tsugaru warm gyre. *Ocean Hydrodynamics of the Japan and East China Sea*, T. Ichiye, Ed., D. Reidel, 225–238..
- Kennelly, M. A., R. H. Evans, and T. M. Joyce, 1985: Small-scale cyclones on the periphery of a Gulf Stream warm-core ring. *J. Geophys. Res.*, **90**, 8845–8857..
- Killworth, P. D., 1983: On the motion of isolated lenses on a beta-plane. *J. Phys. Oceanogr.*, **13**, 368–376.. [Find this article online](#)
- Kubokawa, A., 1991: On the behavior of outflows with low potential vorticity from a sea strait. *Tellus*, **43A**, 168–176..
- Lacombe, H., and C. Tchernia, 1972: Caractères hydrologiques et circulation des eaux en Méditerranée. *The Mediterranean Sea*, D. J. Stanley, Ed., Dowden, Hutchinson, and Ross, 26–36..
- Nof, D., 1978a: On geostrophic adjustment in sea straits and wide estuaries: Theory and laboratory experiments. Part I: One-layer system. *J. Phys. Oceanogr.*, **8**, 690–702.. [Find this article online](#)
- 1978b: On geostrophic adjustment in sea straits and wide estuaries: Theory and laboratory experiments. Part II: Two-layer system. *J. Phys. Oceanogr.*, **8**, 861–872.. [Find this article online](#)
- 1981: On the dynamics of equatorial outflows with application to the Amazon's basin. *J. Mar. Res.*, **39**, 1–29..
- 1986: Geostrophic shock waves. *J. Phys. Oceanogr.*, **16**, 886–901.. [Find this article online](#)
- 1988: Outflows dynamics. *Geophys. Astrophys. Fluid Dyn.*, **40**, 165–193..
- 1993: Generation of ringlets. *Tellus*, **45**, 299–310..
- 1996: What controls the origin of the Indonesian throughflow? *J. Geophys. Res.*, **101**, 12 301–12 314..
- Orlanski, I., 1976: A simple boundary condition for unbounded hyperbolic flows. *J. Comput. Phys.*, **21**, 251–269..
- Perkins, H., T. Kinder, and P. La Violette, 1990: The Atlantic inflow in the western Alboran Sea. *J. Phys. Oceanogr.*, **20**, 242–263.. [Find this article online](#)

- Pichevin, T., 1996: Curving and retroflecting currents: A new eddy generation process. Ph.D. thesis, University of Paris, 124 pp.
- and D. Nof, 1997: The momentum imbalance paradox. *Tellus*, **49**, 298–319..
- Preller, R. H., 1986: A numerical model study of the Alboran Sea gyre. *Progress in Oceanography*, Vol. 16, Pergamon, 113–146..
- Saint-Guilly, B., 1957: Les méandres des veines de courant dans les océans. *Bull. Inst. Océanogr.*, **1108**, 1–11..
- Speich, S., G. Madec, and M. Crépon, 1996: A strait outflow circulation process study: The case of the Alboran Sea. *J. Phys. Oceanogr.*, **26**, 320–340.. [Find this article online](#)
- Viúdez, Á., 1997: An explanation for the curvature of the Atlantic jet past the Strait of Gibraltar. *J. Phys. Oceanogr.*, **27**, 1804–1810.. [Find this article online](#)
- and R. L. Haney, 1997: On the relative vorticity of the Atlantic jet in the Alboran Sea. *J. Phys. Oceanogr.*, **27**, 175–185.. [Find this article online](#)
- , J. Tintoré, and R. L. Haney, 1996: Circulation in the Alboran Sea as determined by quasi-synoptic hydrographic observations. Part I: Three-dimensional structure of the two anticyclonic gyres. *J. Phys. Oceanogr.*, **26**, 684–705.. [Find this article online](#)
- Werner, F. E., A. Cantos-Figuerola, and G. Parrilla, 1988: A sensitivity study of reduced-gravity channel flows with application to the Alboran Sea. *J. Phys. Oceanogr.*, **18**, 373–383.. [Find this article online](#)
- Whitehead, J. A., and A. R. Miller, 1979: Laboratory simulation of the gyre in the Alboran Sea. *J. Geophys. Res.*, **84**, 3733–3742..
- Yasuda, I., K. Okuda, M. Hirai, Y. Ogawa, H. Kudoh, S. Fukushima, and K. Mizuno, 1988: Short-term variations of the Tsugaru Warm Current in autumn. *Bull. Tohoku Reg. Fish. Res. Lab.*, **50**, 153–191..

## List of Symbols

1.  $B_*$  known nondimensional upstream Bernoulli along the right channel wall
2.  $f$  Coriolis parameter ( $f_0 + \beta y$ )
3.  $g'$  “reduced gravity” ( $\Delta\rho/\rho$ ) $g$
4.  $h$  thickness of light water
5.  $\hat{h}_g$  gyre maximum depth
6.  $H$  upstream current depth next to the right wall (looking downstream)
7.  $H_l$  near-wall depth of alongshore current
8.  $L$  alongshore current width
9.  $Q$  mass flux out of the channel
10.  $Q_*$  nondimensional mass flux out of the channel
11.  $r, \theta$  polar coordinates
12.  $R$  gyre diameter
13.  $R_d$  Rossby radius of the channel flow,  $(g'H)^{1/2}/f$
14.  $R_{dg}$  Rossby deformation radius of the gyre
15.  $S$  integration area
16.  $u, \mathbf{v}$  velocities in Cartesian coordinates

17.  $\mathbf{u}_\theta$  orbital velocity in the gyre
18.  $U$  upstream velocity along the right bank
19.  $V$  near-wall speed of the alongshore current
20.  $W$  width of channel
21.  $x_p^*, y_p^*, u_p^*, \mathbf{v}_p^*, h_l^*$  scaled variables associated with the steady alongshore current on the right
22.  $x_g^*, y_g^*, \psi_g^*, h_g^*$  scaled variables associated with the gyres on the left
23.  $\beta$  variation of the Coriolis parameter with latitude
24.  $\epsilon$  small parameter equal to  $\beta R_d / f_0$
25.  $\Phi$  boundary of integration area  $S$
26.  $\rho, \Delta\rho$  density and density difference between the layers
27.  $\nu$  gyre viscosity coefficient
28.  $\Psi$  streamfunction (defined by  $\partial\Psi/\partial y = -uh$ ;  $\partial\Psi/\partial x = \mathbf{v}h$ )

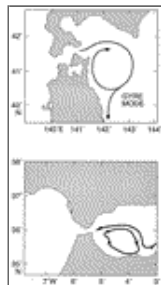
## Tables

Table 1. A description of the (main) six numerical simulations. The mean radius of the gyre is defined as the square root of the gyre area (i.e., the area between the mouth and the point where the radius of curvature of the outermost depth contour reaches a minimum) divided by  $\pi$ . In expt 5, the initial cyclonic vorticity at the mouth corresponds to a velocity profile with about  $0.4 \text{ m s}^{-1}$  along the left channel bank,  $2.7 \text{ m s}^{-1}$  along the right bank, and about  $1.0 \text{ m s}^{-1}$  along the central axis.

Exp.	Parameters	Openness relative to the ocean (see text)	Ratio of gyre's maximum depth to channel depth	Physical Mean value: Density (kg m <sup>-3</sup> )	Physical Mean value: Viscosity (m <sup>2</sup> s <sup>-1</sup> )	Physical Mean value: Coriolis parameter (s <sup>-1</sup> )	Reference (1996)
1	$\beta = 10^{-4} \text{ s}^{-1} \text{ m}^{-1}$ , $\epsilon = 0.1$ $\Delta\rho = 10^{-4} \text{ kg m}^{-3}$ , $\nu = 10^{-4} \text{ m}^2 \text{ s}^{-1}$ $\rho = 10^3 \text{ kg m}^{-3}$ , $W = 10^3 \text{ m}$ $\Phi = 10^3 \text{ m}$	(5.2): anticyclonic and well mixed circulation for the entire channel	$R_d/R_c = 0.75 < 1$	1000	10 <sup>-4</sup>	10 <sup>-2</sup>	11
2	$\beta = 10^{-4} \text{ s}^{-1} \text{ m}^{-1}$ , $\epsilon = 0.1$ $\Delta\rho = 10^{-4} \text{ kg m}^{-3}$ , $\nu = 10^{-4} \text{ m}^2 \text{ s}^{-1}$ $\rho = 10^3 \text{ kg m}^{-3}$ , $W = 10^3 \text{ m}$ $\Phi = 10^3 \text{ m}$	(5.2): anticyclonic for the entire channel	$R_d/R_c = 1.2 > 1$	1000	10 <sup>-4</sup>	10 <sup>-2</sup>	Understand the role of the channel
3	$\beta = 10^{-4} \text{ s}^{-1} \text{ m}^{-1}$ , $\epsilon = 0.1$ $\Delta\rho = 10^{-4} \text{ kg m}^{-3}$ , $\nu = 10^{-4} \text{ m}^2 \text{ s}^{-1}$ $\rho = 10^3 \text{ kg m}^{-3}$ , $W = 10^3 \text{ m}$ $\Phi = 10^3 \text{ m}$	(5.2): anticyclonic for the entire channel	$R_d/R_c = 1.1 > 1$	1000	10 <sup>-4</sup>	10 <sup>-2</sup>	Understand the role of the channel
4	$\beta = 10^{-4} \text{ s}^{-1} \text{ m}^{-1}$ , $\epsilon = 0.1$ $\Delta\rho = 10^{-4} \text{ kg m}^{-3}$ , $\nu = 10^{-4} \text{ m}^2 \text{ s}^{-1}$ $\rho = 10^3 \text{ kg m}^{-3}$ , $W = 10^3 \text{ m}$ $\Phi = 10^3 \text{ m}$	(5.2): anticyclonic and well mixed circulation for the entire channel	$R_d/R_c = 0.8 < 1$	1000	10 <sup>-4</sup>	10 <sup>-2</sup>	12
5	$\beta = 10^{-4} \text{ s}^{-1} \text{ m}^{-1}$ , $\epsilon = 0.1$ $\Delta\rho = 10^{-4} \text{ kg m}^{-3}$ , $\nu = 10^{-4} \text{ m}^2 \text{ s}^{-1}$ $\rho = 10^3 \text{ kg m}^{-3}$ , $W = 10^3 \text{ m}$ $\Phi = 10^3 \text{ m}$	(5.2): anticyclonic and well mixed circulation for the entire channel	$R_d/R_c = 0.8 < 1$	1000	10 <sup>-4</sup>	10 <sup>-2</sup>	Understand the role of the channel
6	$\beta = 10^{-4} \text{ s}^{-1} \text{ m}^{-1}$ , $\epsilon = 0.1$ $\Delta\rho = 10^{-4} \text{ kg m}^{-3}$ , $\nu = 10^{-4} \text{ m}^2 \text{ s}^{-1}$ $\rho = 10^3 \text{ kg m}^{-3}$ , $W = 10^3 \text{ m}$ $\Phi = 10^3 \text{ m}$	(5.2): anticyclonic and well mixed circulation for the entire channel	$R_d/R_c = 0.8 < 1$	1000	10 <sup>-4</sup>	10 <sup>-2</sup>	4
7	$\beta = 10^{-4} \text{ s}^{-1} \text{ m}^{-1}$ , $\epsilon = 0.1$ $\Delta\rho = 10^{-4} \text{ kg m}^{-3}$ , $\nu = 10^{-4} \text{ m}^2 \text{ s}^{-1}$ $\rho = 10^3 \text{ kg m}^{-3}$ , $W = 10^3 \text{ m}$ $\Phi = 10^3 \text{ m}$	(5.2): anticyclonic and well mixed circulation for the entire channel	$R_d/R_c = 0.8 < 1$	1000	10 <sup>-4</sup>	10 <sup>-2</sup>	4
8	$\beta = 10^{-4} \text{ s}^{-1} \text{ m}^{-1}$ , $\epsilon = 0.1$ $\Delta\rho = 10^{-4} \text{ kg m}^{-3}$ , $\nu = 10^{-4} \text{ m}^2 \text{ s}^{-1}$ $\rho = 10^3 \text{ kg m}^{-3}$ , $W = 10^3 \text{ m}$ $\Phi = 10^3 \text{ m}$	(5.2): anticyclonic and well mixed circulation for the entire channel	$R_d/R_c = 0.8 < 1$	1000	10 <sup>-4</sup>	10 <sup>-2</sup>	4

Click on thumbnail for full-sized image.

## Figures



Click on thumbnail for full-sized image.

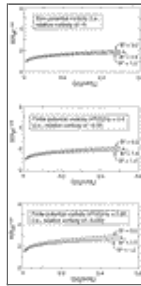
Fig. 1. The Tsugaru (top panel) and the Alboran (bottom panel) gyres (adapted from [Conlon 1982](#) and [Viúdez et al. 1996](#)).





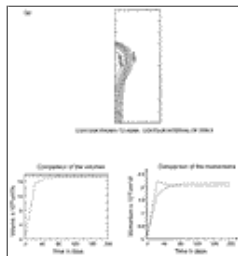
Click on thumbnail for full-sized image.

Fig. 2. Schematic diagram of the model under study. An eastward channel carrying water with density ( $\rho$ ) empties into an otherwise stagnant ocean with density ( $\rho + \Delta\rho$ ). The streamlines in the channel are assumed to remain parallel to the channel walls until the coastline is reached (i.e., section AB). Assuming (and later verifying with the numerical simulations) that there is an inviscid steady state corresponding to the current hugging the coastline on the right-hand side, one finds that the momentum imparted on the region bounded by ABCDEFA by the water exiting through CD is balanced by the southward  $\beta$  force associated with the gyre. Without loss of generality we may choose  $\psi = 0$  along the front ( $h = 0$ ).



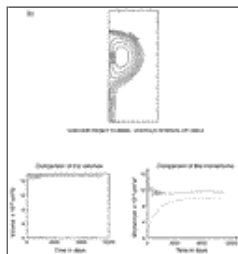
Click on thumbnail for full-sized image.

Fig. 3. The gyre radius ( $R$ ) as a function of the channel discharge ( $Q$ ) for zero and finite potential vorticity flow. Note that  $Q^* \leq \frac{1}{2}$  because along the left bank  $h^* \geq 0$ . For  $Q^* = \frac{1}{2}$ , the depth near the left wall vanishes and the structure of the flow in the channel is identical to that of the alongshore current. The cases correspond to an upstream flow with negative relative vorticity that is strong enough to form the gyre (i.e., friction plays no role in the establishment of the gyres):  $h^{(0)}(0)$  is the gyre's zeroth-order depth in the center and  $H_p$  is the potential vorticity depth.



Click on thumbnail for full-sized image.

Fig. 4a. Numerical simulation of experiment 1. Depth contours (in centimeters) for the steady state are shown in the upper panel, and a comparison of the volumes and momentum fluxes at the entrance and exit are shown in the lower panels. The momentum fluxes correspond to the two terms associated with Eq. (3.4). (The southern edge of the gyre was defined to be the point where the radius of curvature of the outermost contour reaches a minimum.) Note that a steady state is reached within 80 days. Basin size is  $750 \times 300 \text{ km}^2$ . In the lower panels, the dashed lines denote the downstream current; the solid line the inflow, and the dotted line  $\beta$ .



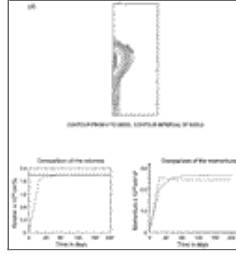
Click on thumbnail for full-sized image.

Fig. 4b. As in Fig. 4a except that the variables are those of experiment 2; basin size is  $1200 \times 525 \text{ km}^2$ . Again, the dashed lines denote the downstream current, the solid line the inflow, and the dotted line  $\beta$ . Here, a steady state is reached much later (4000 days) because the upstream relative vorticity is weakly anticyclonic (see Table 1) so that the potential vorticity has to be altered (by friction) and this takes time.



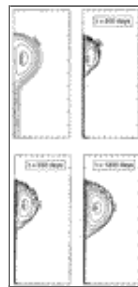
Click on thumbnail for full-sized image.

Fig. 4c. As in Fig. 4b except that the shown variables are those of experiment 3. Basin size is  $975 \times 675 \text{ km}^2$ . Again, the alteration of potential vorticity is slow so that a steady state is reached later than it is in the no alteration case.



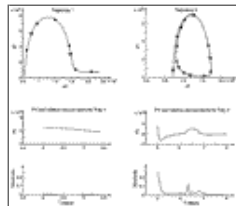
Click on thumbnail for full-sized image.

Fig. 4d. As in Fig. 4a except that the variables are associated with experiment 5. Basin size is  $750 \times 300 \text{ km}^2$ . Here again, there is also an alteration of potential vorticity but it is completed quickly due to large shear at the exit. Consequently, a steady state is reached relatively fast (within 80 days).



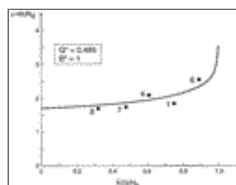
Click on thumbnail for full-sized image.

Fig. 5. Potential vorticity contours (within the gyre) associated with expt 2 (in  $\text{cm}^{-1} \text{ s}^{-1}$ ). For a comparison the (steady) depth contours are also shown (upper-left panel). Note that the potential vorticity alteration takes place first in the center of the gyre (after 200 days the nondimensional potential vorticity is  $1.5 \times 10^{-9}$ , after 550 days it is  $1.3 \times 10^{-9}$ , and after 1200 days it is  $1.1 \times 10^{-9}$ ); it then propagates outward. Basin size is  $1200 \times 525 \text{ km}^2$ .



Click on thumbnail for full-sized image.

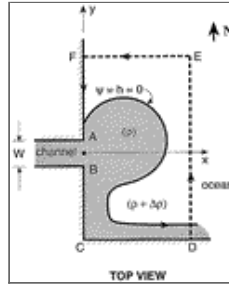
Fig. 6. Trajectories of two particles (upper panel) and the associated changes in potential vorticity (central panels) in expt 5. Particle 1 (left panels) is situated outside the gyre and ends up in the downstream current, whereas particle 2 (right panel) is trapped in the gyre. Times corresponding to every 20 000 s are indicated with solid dots. The lower panel represents the importance of friction as a function of time. The parameter viscosity–vorticity (shown on the vertical axis of the lower panel) is defined by  $[(F_x^2 + F_y^2)/(f_x^2 + f_y^2)]^{1/2}$ , where  $F_x$  and  $F_y$  are the frictional terms and  $f_x$  and  $f_y$  are the Coriolis terms in the  $x$  and  $y$  directions. It is a global measure of the importance of viscosity. Note that particle 2 experiences a dramatic reduction in its potential vorticity (due to friction), whereas particle 1 experiences no such reduction. To assure the accuracy of our results, the resolution was increased in this particular experiment; the grid space was 1 km, the time step 100 s and the viscosity  $2 \times 10^6 \text{ m}^2 \text{ s}^{-1}$ . The first particle was released 11 km from the right bank of the channel whereas the second was released 2 km from the bank. Both were released after 5 days of integration (to assure completion of the initial adjustment).



Click on thumbnail for full-sized image.

Fig. 7. A comparison of the inviscid analytical prediction for the gyre's mean radius (solid curve) with the numerical experiments with no potential vorticity alteration (experiments 1, 4, 6, 7, and 8). (A comparison of the above analytical results to

the other numerical experiments is meaningless as the analytical predictions are not valid when the potential vorticity is altered.) Recall that  $\bar{h}(0)$  is the depth at the center of the gyre and  $H_p$  is the “potential vorticity depth.” Given the approximations involved in our analytical model the agreement is excellent. As expected, the largest error (11%) is associated with experiment 1 where the shape distortion (from a circle) is the largest (Fig. 4a). Note that the mean numerical radius was defined as the square root of the gyre’s area (i.e., the area between the mouth and the point where the radius of curvature of the outermost depth contour reaches a minimum) divided by  $\pi$ .



Click on thumbnail for full-sized image.

Fig. 8. A gyre with a wall on the southern side. Here, the wall alters the detailed structure of the gyre but does not alter the main reason for its formation (see text).



Click on thumbnail for full-sized image.

Fig. 9. The establishment of the gyre when a southern wall is added to the basin. The shown steady states correspond to a wall situated away from the gyre (left panel), at the edge of the gyre (center panel), and at the center (right panel). Clearly, the presence of the zonal wall does not prevent the establishment of the gyre even though a force is exerted on it (see text). The parameters are the same as those used in experiment 1. Basin sizes are:  $750 \times 375 \text{ km}^2$  (upper panel),  $600 \times 375 \text{ km}^2$  (lower-left panel), and  $450 \times 375 \text{ km}^2$  (lower-right panel). Contours are given in centimeters.

<sup>1</sup> It may not be entirely obvious to the reader that an anticyclonic gyre requires a *core* with anticyclonic vorticity. To see this, consider the relative vorticity in polar coordinates  $(1/r)(d/dr)(r\mathbf{v}_\theta)$  and assume, for the moment, that it is constant (say,  $A$ ). It is easy to show that, under such conditions,  $\mathbf{v}_\theta = Ar/2 + C/r$  (where  $C$  is an integration constant). The requirement of zero speed at the center implies that  $C$  must be zero and the requirement that  $\mathbf{v}_\theta < 0$  implies that  $A < 0$ .

Corresponding author address: Prof. Doron Nof, Department of Oceanography (4320), The Florida State University, Tallahassee, FL 32306-4320.

E-mail: [nof@ocean.fsu.edu](mailto:nof@ocean.fsu.edu)

top ▲



© 2008 American Meteorological Society [Privacy Policy and Disclaimer](#)  
 Headquarters: 45 Beacon Street Boston, MA 02108-3693  
 DC Office: 1120 G Street, NW, Suite 800 Washington DC, 20005-3826  
[amsinfo@ametsoc.org](mailto:amsinfo@ametsoc.org) Phone: 617-227-2425 Fax: 617-742-8718  
[Allen Press, Inc.](#) assists in the online publication of AMS journals.